The contrasting effects of thermodynamic and dynamic processes on East Asian summer monsoon precipitation during the Last Glacial Maximum: a data-model comparison

Yong Sun[1,2] · Haibin Wu[3,4,5] · Masa Kageyama[2] · Gilles Ramstein[2] · Laurent Z. X. Li[6] · Ning Tan[3] · Yating Lin[3] · Bo Liu[7,1] · Weipeng Zheng[1,8] · Wenchao Zhang[3] · Liwei Zou[1] · Tianjun Zhou[1,9]

Abstract

The Last Glacial Maximum (LGM; 21 ka BP) was the most recent glacial period when the global ice sheet volume was at a maximum. Therefore, the LGM can be used to investigate atmospheric dynamics under a climate that differed significantly from the present. This study quantitatively compares pollen records of boreal summer (June–July–August) precipitation with the PMIP3 LGM simulations. The data-model comparison shows an overall agreement on a drier than pre-industrial East Asian summer monsoon (EASM) climate. Nevertheless, 17 out of 55 records show a regional precipitation increase that is also simulated over the additional land mass area due to sea level drop. The thermodynamic and dynamic responses are analyzed to explain a drier LGM EASM as a combination of these two antagonistic mechanisms. Relatively low atmospheric moisture content was the main thermodynamic control on the lower LGM (relative to pre-industrial levels) EASM precipitation amounts in both the reconstructions and the models. In contrast, two dynamic processes in relation to stationary eddy activity act to increase EASM precipitation regionally in records and simulations, respectively. Precipitation increase in records is explained by dynamic enhancement of the horizontal moisture transport, while dynamic enhancement of the vertical moisture transport leads to simulated precipitation increase over the specific region where landmass was exposed during LGM along continental coastlines of China due to significant drop in sea level (relative to pre-industrial levels). Overall, the opposing effects of thermodynamic and dynamic processes on precipitation during the LGM provide a means to reconcile the spatial heterogeneity of recorded precipitation changes in sign, although data-model comparison suggests that the simulated dynamic wetting mechanism is too weak relative to the thermodynamic drying mechanism over data-model disagreement regions.

✉ Yong Sun
    sunyong@mail.iap.ac.cn

Extended author information available on the last page of the article

Key Points

Quantitative data-model comparison of EASM precipitation shows an overall agreement on a drier China

Distinct regions for precipitation increase in data and model

Decrease in EASM precipitation in data and model regulated by thermodynamic processes

Increase in EASM precipitation in data and model due to two different stationary eddy related dynamic processes

1 Introduction

The Last Glacial Maximum (~ 21 ka BP, LGM) was the most recent glacial period, when global ice sheets reached a maximum extent and the global sea level was ~130 m±5 lower than present (Clark and Mix 2002; Clark et al. 2009). Both the presence of large Northern Hemisphere ice sheets and low atmospheric CO_2 concentrations (~180–185 ppmv compared with 280 ppmv during the pre-industrial period) contributed to the LGM being cooler than the pre-industrial period (Monnin et al. 2001; Jahn et al. 2005; Liu et al. 2002). Thus, the LGM provides an ideal opportunity to study the interactions between ice sheets and climate (Clark et al. 1999), and investigate how the Earth system responds to CO_2 concentrations that are below present levels (Peteet 2018).

Global and regional paleo-datasets documenting the spatial climatic patterns during the LGM have been assembled in recent decades with a specific focus on quantitative paleoclimatic reconstruction (CLIMAP 1976; Farrera et al. 1999; MARGO 2009; Bartlein et al. 2011; Shakun et al. 2012). Such reconstructions are crucial for evaluating changes in the Earth's climate system on different time scales. However, reconstructions based on proxy data alone cannot explain how the dynamic mechanisms behind climate changes at the LGM.

As the most recent extreme cold and dry period in the last glacial–interglacial cycle during the Quaternary, the LGM has been one of the foci of the Paleoclimate Modelling Intercomparison Project (PMIP) since its inception (Kageyama et al. 2017). This has enabled the evaluation of model performance with respect to the LGM climate changes using paleoclimate data (Kageyama et al. 2001, 2006; Ramstein et al. 2007; Wu et al. 2007; Braconnot et al. 2012; Harrison et al. 2015; Chevalier et al. 2017), and an improved understanding of the large-scale dynamics of the LGM climate changes (Otto-Bliesner et al. 2006; Braconnot et al. 2007a, b; Kageyama et al. 2013; Cao et al. 2019).

In addition to the study of large-scale climate responses, there have been increasing attempts to use modern methods of climate dynamic diagnosis to uncover the underlying mechanisms associated with regional climate changes under paleoclimate conditions (Ludwig et al. 2019; Zheng et al. 2004). For example, one recent study used a weather typing approach to point out regional differences in the precipitation patterns over Europe under the LGM climate condition and their linkage to the North Atlantic storm track (Ludwig et al. 2016). Other studies investigated genesis potential indices as factors for tropical cyclone formation in simulations of the LGM (Korty et al. 2012; Yan and Zhang 2017). Another powerful tool is the water vapor budget that can be used to improve our understanding of physical processes associated with monsoon precipitation changes under past warm/cold climatic conditions, which are related to the sources and sinks of water vapor content in the atmospheric column (Sun et al. 2016, 2018; Burls and Fedorov 2017; Yanase and Abe-Ouchi 2007; Yan et al. 2016; Adam et al. 2019). Changes to the East Asian summer monsoon (EASM) at the LGM have been widely characterized as a reduction in precipitation (Jiang et al. 2015; Lu et al. 2013) with a weakening in the monsoon circulation intensity (Jiang and Lang 2010). However, the relative contributions of thermodynamic and dynamic processes to EASM precipitation decline during the LGM remain unknown.

In this study, we first provide a quantitative data-model comparison of the summer monsoon climate changes over China during the LGM period. We then clarify the opposing roles of thermodynamic and dynamic processes in EASM precipitation decline using the decompositions of the water vapor budget. Finally, we unveil the underlying physics of these two contrasting processes.

2 Materials and methods

2.1 Pollen-based reconstruction

Fossil pollen records provide evidence of changes in vegetation distribution over time, which are accessible sources for quantitative spatial paleoclimate reconstructions. In this study, we systematically collected fossil pollen datasets over China (35 new pollen sites) for the LGM period published in the last decade, to replenish the Chinese Quaternary Pollen Database (33 original pollen sites) (MCQPD 2000).

An Inverse Vegetation Model (IVM) is used for our paleoclimate reconstruction (Guiot et al. 2000; Wu et al. 2007), which is based on the physiological-process

vegetation model BIOME4 (Kaplan 2001). The principle behind this method is that we can attempt to estimate the inputs for the vegetation model (i.e., the seasonal climate) if we know the information related to the output of the model (i.e., biome scores at pollen site). IVM makes it possible to reconstruct seasonal climates for the LGM, therefore it increases the reliability of pollen-based reconstructions. The method has been validated in Eurasia, Africa (Guiot et al. 2000; Wu et al. 2007; Lin et al. 2019) and North America (Izumi and Bartlein 2016). The IVM method is based on a total distance between the simulated biome scores and pollen biome scores; although sometimes the total distance is the minimum value, the predicted biome is not the target pollen biome. Here 81% of the biomes at pollen sites (55 sites/68 total sites) are correctly predicted and thus successfully reconstructed for the paleoclimate in China. This new dataset significantly improves the spatial distribution of pollen records in China, and thus enhances paleoclimatic reconstruction during the LGM as demonstrated by the work of Wu et al. (2019). All the reconstructed paleoclimate values including annual and summer precipitation in Supplementary Table S1 are the rainfall anomaly between the LGM and the pre-industrial (PI) period over China and more detail information on the IVM method can be found in Wu et al. (2019).

2.2 PMIP3 simulations

LGM simulations involved in the PMIP Phase 3 (PMIP3) framework were used to quantitatively compare model results with reconstructions and provide a useful understanding of EASM precipitation changes between the LGM and the preindustrial period. The LGM simulations follow the common PMIP3 protocol (Braconnot et al. 2012). Compared with pre-industrial levels, this stipulated a sea level that was 130 m lower, lower greenhouse gas concentrations (185 ppm for atmospheric CO_2, 350 ppb for CH_4, and 200 ppb for N_2O), a blended CMIP5/PMIP3 ice sheet configuration (Abe-Ouchi et al. 2015), and small changes in global mean insolation. Nine models are used in this study, for which the complete set of monthly variables needed to conduct water vapor and moist static energy budget analysis are currently available online (Table S2). For each model, the last 30 years of LGM and pre-industrial simulations are analyzed. All model outputs are interpolated from the original horizontal model grid to a horizontal grid of 2.5° in latitude by 2.5° in longitude before calculating the multi-model ensemble (MME) mean. These nine models are able to reproduce the present-day EASM climate as demonstrated in Sun et al. (2018; Fig. S1).

2.3 Diagnostic methodology

We used the water vapor budget equation to investigate physical processes associated with the simulated response of EASM precipitation to LGM cooling (Trenberth and Guillemot 1995). Neglecting the tendency term in the steady state, column-integrated moisture budget equation can be expressed:

$$P = E - \langle \omega \partial_P q \rangle - \langle \vec{V}_H \bullet \nabla q \rangle + Res \tag{1}$$

where P is precipitation, E is evaporation, ω is the vertical velocity at a constant pressure coordinate, q is the atmospheric specific humidity, $\vec{V}_H$ is horizontal wind, and Res is a residual term due to variation of submonthly transient eddies (Li and Ting 2017). The angle brackets indicate that the variables in Eq. 1 are integrated across the pressure (p) levels throughout the troposphere (Chou and Lan 2012). Changes in precipitation amounts (δP) through the LGM can be derived from Eq. 1 as follows:

$$\delta P = \delta E - \delta \langle \omega \partial_P q \rangle - \delta \langle \vec{V}_H \bullet \nabla q \rangle - \delta Res \tag{2}$$

To further examine the relative contributions of changes in specific humidity and atmospheric circulation to changes in precipitation, both (horizontal and vertical) advection terms in Eq.2 were further decomposed into: (1) thermodynamic contribution (TC) caused by changes in specific humidity with unchanged circulation, (2) dynamic contribution (DC) from atmospheric circulation changes with unchanged specific humidity, and (3) non-linear (NL) effects related to simultaneous changes in atmospheric circulation and specific humidity (Seager et al. 2010).

Within such a decomposition framework, the horizontal advection of humidity $-\langle \vec{V}_H \bullet \nabla q \rangle$ can be written as:

$$TC = -\langle \vec{V}_H \bullet \nabla \delta q \rangle = -\frac{1}{g \rho_w} \int_0^{P_s} \vec{V}_H \bullet \nabla \delta q \, dp \tag{3}$$

$$DC = -\langle \delta \vec{V}_H \bullet \nabla q \rangle = -\frac{1}{g \rho_w} \int_0^{P_s} \delta \vec{V}_H \bullet \nabla q \, dp \tag{4}$$

$$NL = -\langle \delta \vec{V}_H \bullet \nabla \delta q \rangle = -\frac{1}{g \rho_w} \int_0^{P_s} \delta \vec{V}_H \bullet \nabla \delta q \, dp \tag{5}$$

where ρ_w is the density of water, g is gravity. Similarly, the vertical advection $-\langle \omega \partial_P q \rangle$ is also decomposed into TC and DC and NL:
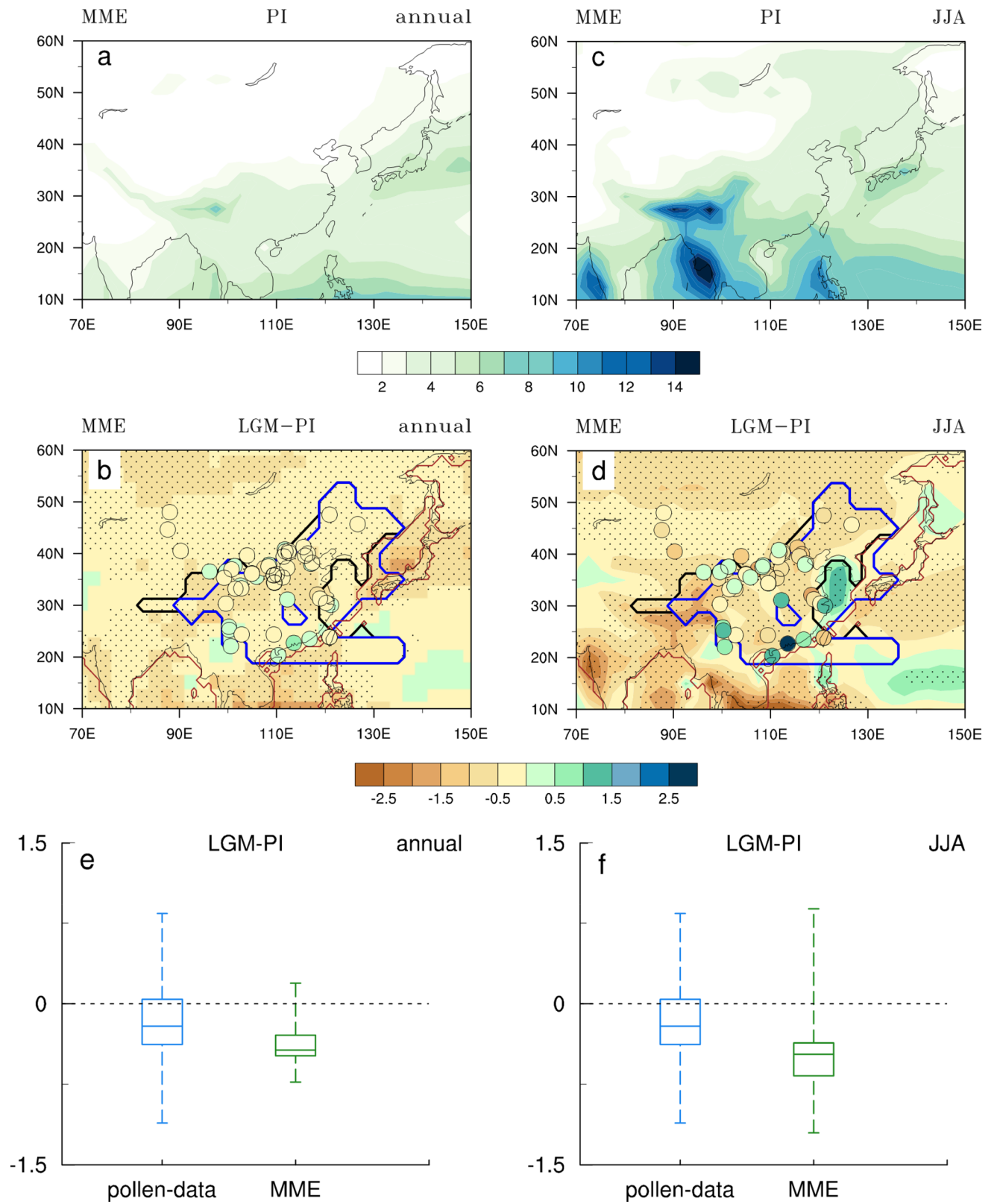
◄**Fig. 1** Precipitation (mm/day) for PI (preindustrial, top) and the change (middle and bottom) from LGM (last glacial maximum) to PI for the annual mean (left panels) and boreal summer mean (June–July–August, JJA; right panels). All panels are based on MME (multi-model ensemble) from PMIP simulations. Dotted zones at middle panels are statistically significant at 99% confidence level (Student's t-test). Solid colored circles in the panels of the middle row represent pollen-based precipitation reconstructions for a few available sites. Box-and-whisker plots on bottom panels show the minmum, 25th, 50th, 75th, and maximum of reconstructed and simulated precipitation for annual mean and JJA. The East Asian Summer Monsoon (EASM) domains in PI (black curve) and LGM (blue curve) are also shown in middle panels and Figs. 3, 5, and 6. The land-sea mask in **b-d** during LGM is in brown contour (source: https://wiki.lsce.ipsl.fr/pmip3/doku.php/pmip3:design:21k:final)

$$TC = -\langle \omega \partial_P \delta q \rangle = -\frac{1}{g\rho_w} \int_0^{P_s} \omega \partial_P \delta q dp \qquad (6)$$

$$DC = -\langle \delta \omega \partial_P q \rangle = -\frac{1}{g\rho_w} \int_0^{P_s} \delta \omega \partial_P q dp \qquad (7)$$

$$NL = -\langle \delta \omega \partial_P \delta q \rangle = -\frac{1}{g\rho_w} \int_0^{P_s} \delta \omega \partial_P \delta q dp \qquad (8)$$

Moist static energy (MSE), due to its excellent property of conservation in the atmospheric circulation, can be used to diagnose large-scale and long-term mean atmospheric vertical motion, which is strongly associated to position, intensity and variation of the EASM precipitation (Chen and Bordoni 2014; Sun et al. 2016, 2018). The MSE budget equation, for our purpose of diagnosing atmospheric vertical motion, can be written as follows:

$$\langle \overline{\omega \partial_p MSE} \rangle = \overline{F^{net}} - \overline{\langle V \cdot \nabla E \rangle} \qquad (9)$$

where the overbar "——" indicates the time mean and angle brackets " < > " indicate the vertical integral of the variables in the atmospheric column, $\overline{F^{net}}$ is the net heat flux into the atmospheric column, and E is moist enthalpy. MSE decreases with pressure in the troposphere, which is identified as the physical basis of MSE applied to monsoon precipitation. i.e., ascending (descending) motion results from the diabatic heating (cooling) caused by the combined net effects of $\overline{F^{net}}$ and $-\overline{\langle V \cdot \nabla E \rangle}$.

The definition of the East Asian monsoon domain requires two conditions (Wang et al. 2012): (1) an annual range of precipitation rates exceeding 2 mm/day; and (2) local summer precipitation exceeding 55% of the total annual amount. The annual range of precipitation is defined as the local summer (May–June–July–August–September) minus the local

winter (November–December–January–February–March) precipitation. In addition, given the difference in the EASM domain between the LGM and pre-industrial periods, as well as the inter-model spread of the EASM domain, the moisture budgets of the LGM and pre-industrial periods were calculated based on the EASM domain for each model (Fig. S2).

3 Results

3.1 Proxy data-model comparison over China

To evaluate the consistency of model simulation against proxy data for the LGM EASM region, a data-model comparison over China is displayed in Fig. 1 for annual and seasonal (June–July–August, JJA) precipitation. There is an overall agreement between model and precipitation proxy data in showing general dry conditions in LGM (relative to pre-industrial PI; Fig. 1, top panels) for the whole year and JJA (Fig. 1, bottom panels). There is however an obvious disagreement in southern China and in the southwestern margins of the EASM domain (Fig. 1, middle panels). We can further see that the overall decrease of annual precipitation (Figs. 1b–e) is mainly due to the decrease in summer (Fig. 1d–f), which is consistent with what is reported by Wu et al. (2019). In the following, we will present our diagnostics in terms of thermodynamic and dynamic contributions to variation of precipitation in JJA, which permits us to gain a mechanistic understanding of the precipitation decline in LGM, and to reveal some insights about the regional disagreement of rainfall changes between pollen-based reconstruction and model simulation.

3.2 Decomposition of EASM precipitation changes into thermodynamic and dynamic contributions

We used a decomposition of the water vapor budget to identify relevant physical processes influencing the mean EASM precipitation for LGM, and compared them with the pre-industrial situation. Figure 2a displays the different terms of the water vapor budget equation at equilibrium for both LGM and PI. It can be seen that the precipitation eliminating water vapor from the atmospheric column is mainly balanced by the surface evaporation and the vertical moisture transport, whereas horizontal moisture advection contributes relatively less to the balance of water vapor.

Decreases in evaporation and vertical moisture transport both contributed to EASM precipitation decline during the LGM (Fig. 2b). In contrast, there is large uncertainty in the contributions of horizontal moisture transport to the simulated precipitation decline in the LGM, as manifested by inter-model spread for this term (Fig. 2b). In addition to quantifying the relative contribution of thermodynamic
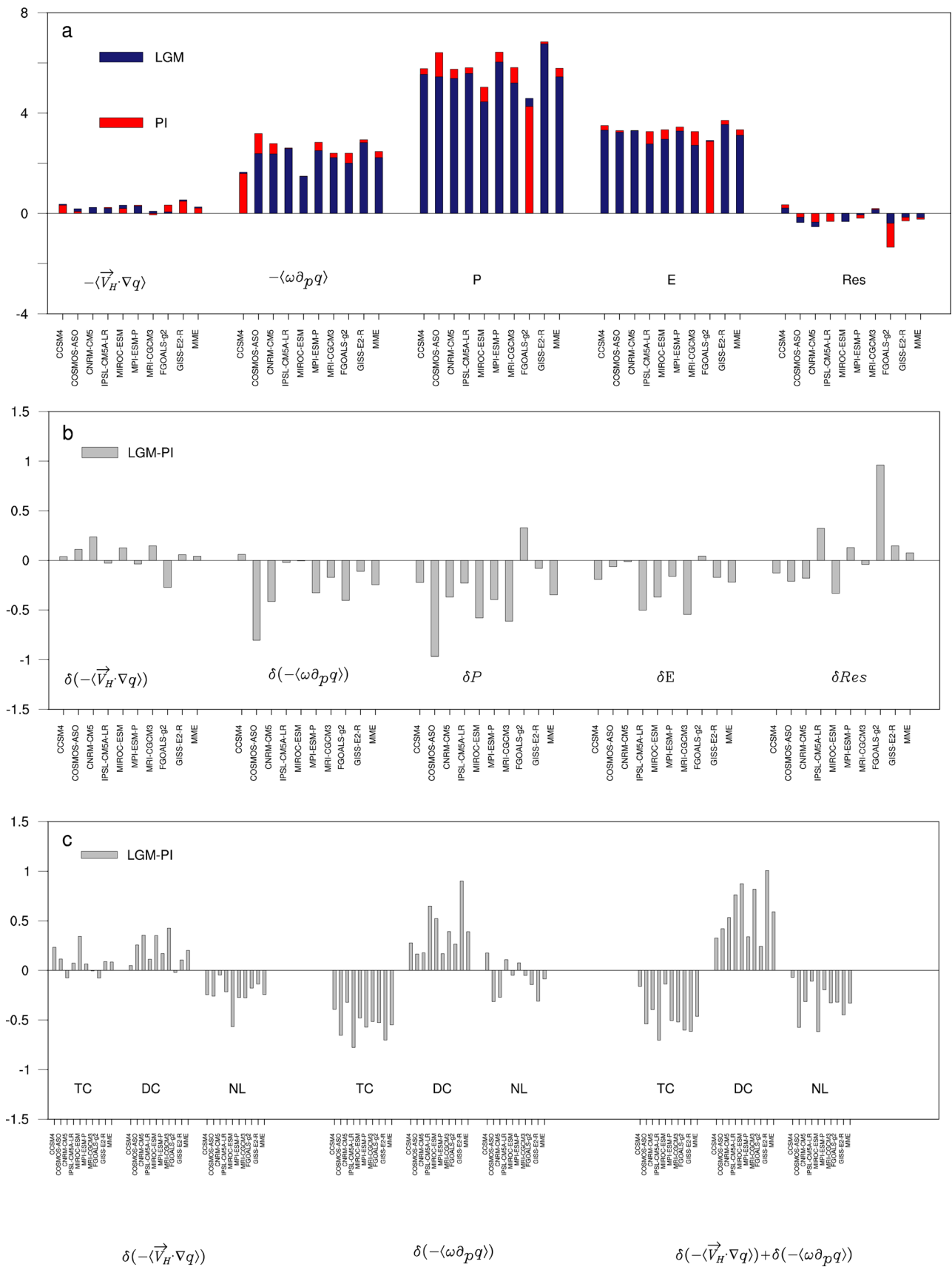
Fig. 2 a Decomposition of water vapor budget equation into its different constituent terms (mm/day, red bars for PI and blue bars for LGM) for JJA seasonal mean in the EASM domain for each of the PMIP models. **b** The same as in panel **a,** but expressed as the difference LGM minus PI. **c** The two advection terms shown in the panel **b,** horizontal advection $\delta\langle -\overline{V}_H \bullet \nabla q\rangle$ and vertical advection $\delta\langle -\omega\partial_P q\rangle$ (also their sum with final results shown at the right end of the panel), decomposed into contributions related to changes in specific humidity with constant circulation (*TC,* thermodynamic contribution) and changes in circulation with constant specific humidity (*DC,* dynamic contribution), and into a non-linear term related to simultaneous changes in specific humidity and circulation (NL, non-linear contribution)

and dynamic processes to the differences in precipitation between the LGM and pre-industrial periods, we completed another decomposition to reveal possible causes of uncertainty in the changes of the horizontal advection term (i.e., TC, DC and NL of $\delta(-\langle\overrightarrow{V}_H \bullet \nabla q\rangle)$). We found the nearly consistent (negative) sign in the change in vertical moisture transport across models (Fig. 2b) mainly results from the contribution from the thermodynamic component (TC), compensated by the dynamic component (DC) (Fig. 2c). Different from effects of TC and DC, the effect of non-linear (NL) processes on vertical moisture transport exhibits large inter-model uncertainty in sign (Fig. 2c). Overall, the inter-model spread associated with changes in horizontal moisture transport (Fig. 2b) is largely the result of divergent impacts of the three processes (Fig. 2c), as manifested by a consistent increase in DC and decrease in NL and slight inter-model spread in sign of TC (Fig. 2c).

The net effect of TC and DC on the enhancement of the horizontal moisture transport is dominated by DC (Fig. 2c). As a whole, the total thermodynamic contribution, which is to weaken the net effect of moisture transport, mainly results from the decrease of vertical moisture transport, whereas the total increase of DC is from both terms of horizontal and vertical moisture transports (Fig. 2c). In addition, the decrease of total NL effect is from that of the horizontal moisture transport (Fig. 2c), which is much weaker than that of TC in vertical moisture transport. This makes TC dominate a decrease of precipitation at the LGM.

Thanks to the decomposition into thermodynamic and dynamic effects, the decrease in vertical moisture transport is revealed to be in relation with thermodynamic processes which are from water vapor changes and are responsible for EASM precipitation decline in LGM. The enhancement of horizontal and vertical moisture transports due to increases in horizontal circulation and vertical motion in the atmosphere is revealed to two dynamic processes that contribute to the increase of precipitation for LGM. To further examine the extent to which those two dynamic processes favor LGM precipitation increase, Fig. 3 shows the spatial distributions of the dynamic terms in shaping horizontal and vertical moisture transports. The total dynamic effect of horizontal

and vertical moisture advections contributes to precipitation increase over most parts of EASM domain (Fig. 3a), There are distinct regions for the dynamic enhancements on the horizonal and vertical moisture advections (Fig. 3b–c). The dynamic enhancement of the horizonal moisture transport is generally significant along the middle and lower Yangtze River (Fig. 3b), while significant enhancement of vertical moisture transport due to the dynamic effect is confined to the regions where the continental coastline of China expanded during LGM (relative to pre-industrial levels) due to a sharp decline in sea level (Fig. 3c).

To examine the role of stationary eddy circulation in dynamic increase in the horizontal and vertical moisture transports, we compared the spatial patterns of dynamic contribution (DC; Fig. 3, left panel) with those of DC due to corresponding stationary eddy component (eddyDC; Fig. 3, right panel). The spatial comparisons show remarkable resemblance regarding DC and eddyDC to changes in two moisture advections (Fig. 3). This finding leads to a dominant control of increased stationary eddy horizontal circulation and vertical motion on the dynamic increase in the horizontal and vertical moisture transports.

3.3 Underlying physics of thermodynamic and dynamic processes

We will now consider the key physical processes involved in regional precipitation formation to uncover the underlying mechanisms associated with the TC and DC that contributed to EASM precipitation changes during the LGM. Here we focus mainly on the thermodynamic control on the decrease in water vapor content in the atmosphere and the dynamical control on moisture advections related to precipitation changes in the LGM.

3.3.1 Decrease of EASM precipitation under thermodynamic control

As the climate cools, the atmospheric moisture content decreases as described by the Clausius–Clapeyron (C–C) equation. The reduction in water vapor in response to LGM cooling contributes to reduced large-scale water vapor supply for EASM precipitation during the LGM (Figs. 4a–b). This is the primary cause of the lower EASM precipitation at the LGM, as compared with the pre-industrial period. Moreover, a regional decrease of water vapor in the atmosphere over East Asia leads to weakened vertical moisture transport during the LGM compared with the pre-industrial climate (Fig. 5a). Thus, a thermally controlled decrease in vertical moisture transport contributed to EASM precipitation decline at the LGM.
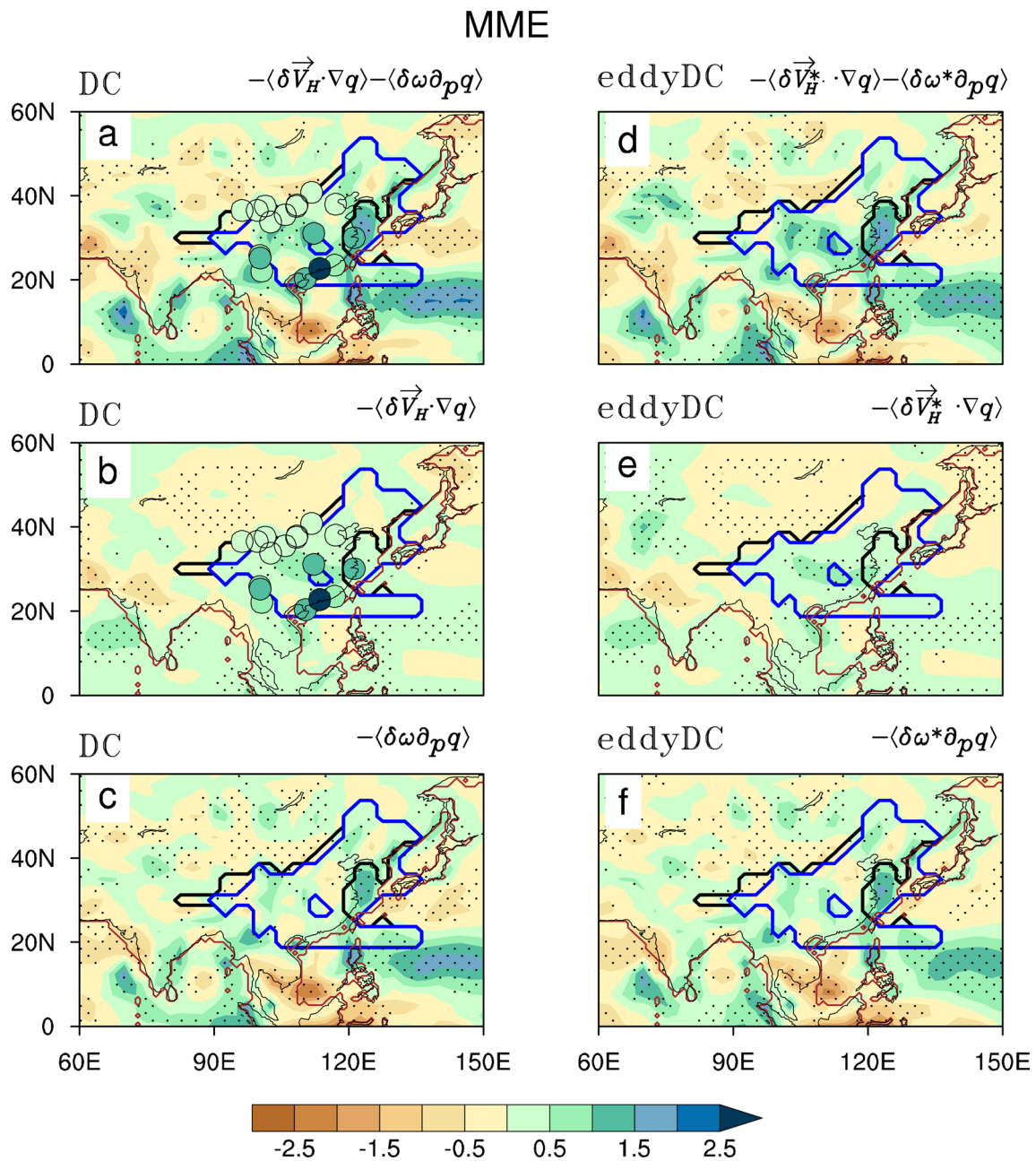
MME

Fig. 3 The MME-based spatial distributions of two dynamic components (DC, left panels) of moisture budget against those of DC in relation to stationary eddy (eddyDC, right panels) in the boreal summer (mm/day). Middle panel: DC and eddyDC of horizontal moisture advection. Bottom panel: DC and eddyDC of vertical moisture advection. Top panel: sum of DC (eddyDC) of horizontal and vertical moisture advections. Stippling denotes regions where the DC in each plot contributes significantly at 5% level (Student's t-test) to moisture advection differences between LGM and PI (Student's t-test). Colored circles are 17 sites of reconstructed LGM precipitation increase in boreal summer compared to PI. Brown contour in each plot is the land-sea mask during LGM

3.3.2 Increase in EASM precipitation regulated by dynamic processes

DC contributes to increase the EASM precipitation during the LGM via different processes based on the regulation of horizontal moisture transport and vertical moisture transport. The DC-related increase in horizontal circulation is largely the result of an enhancement of stationary eddy horizontal circulation over the EASM domain (Fig. 3b), as manifested by enhanced southerly on the southeastern flank of an anomalous cyclone occupying the EASM domain (Fig. 5b). It is reported that ice sheet growth during LGM in the Northern Hemisphere acts to increase stationary eddy meridional velocity (Gao et al. 2020). In essence, we
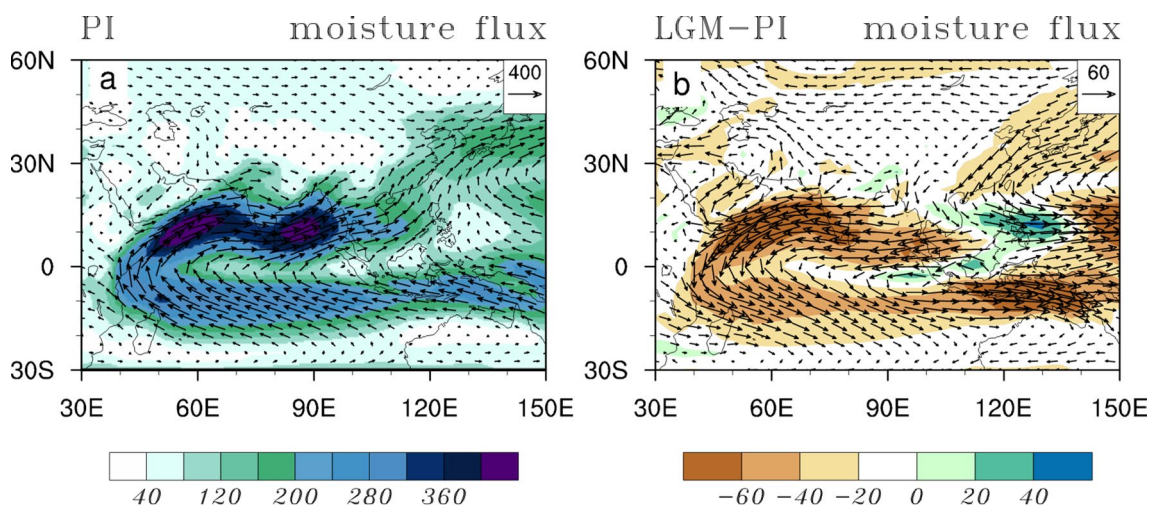
Fig. 4 The MME-based large-scale moisture transport in the boreal summer for (**a**) the PI and (**b**) LGM minus-PI, as represented by vertical integral of moisture flux (units: $kg \cdot m^{-1} \cdot s^{-1}$) throughout the troposphere
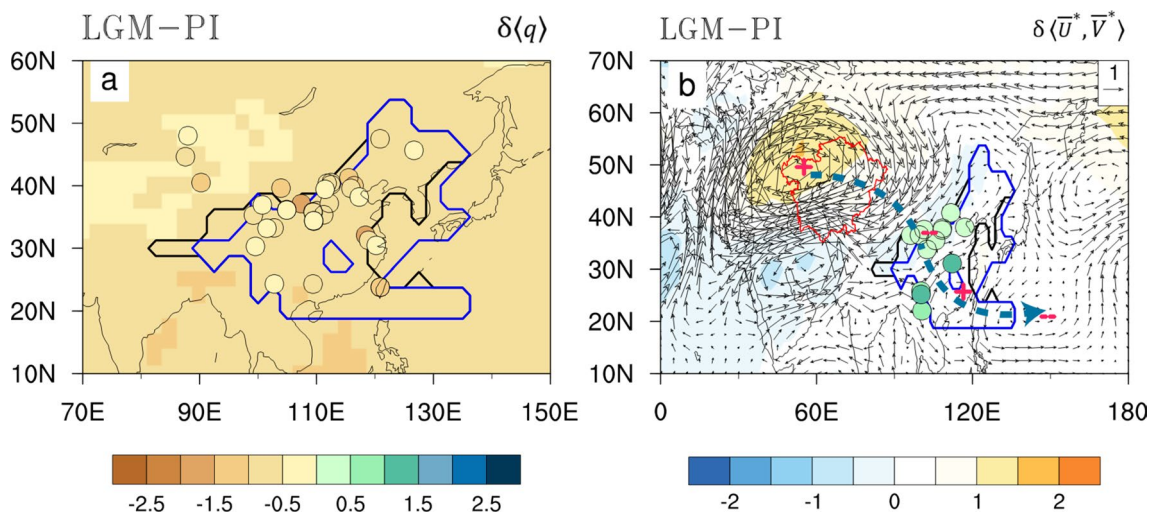

Fig. 5 The MME-based vertical integral of three variables (specific humidity, stationary eddy horizontal circulation and air temperature) in the boreal summer over the troposphere to show differences between LGM and the PI period: (**a**) atmospheric moisture content ($\delta\langle q \rangle$; units: 10^{-3} g·kg^{-1}), (**b**) stationary eddy horizontal circulation ($\delta\langle \overline{U}^*, \overline{V}^* \rangle$; units: m s^{-1}) and stationary eddy air temperature (shading, units: °C). Brown and green circles in a–b indicate 38 and

13 proxy records with precipitation (units: mm/day) decrease and increase, associated with $\delta\langle q \rangle$ decrease and $\delta\langle \overline{U}^*, \overline{V}^* \rangle$ increase over EASM domain, respectively. The red curve in **b** indicates the Central Asia domain (retrieved from http://www.geodoi.ac.cn/WebEn/doi.aspx?Id=1390). The dashed blue line indicates the trajectory of the stationary eddy wave train, which consists of anticyclones (red "+") and cyclones (red "-")

identify this cyclonic anomaly as a part of a wave train structure emanating from a warm-core anticyclone over Central Asia and surrounding regions to a cyclone with southeastern part penetration into EASM domain, then an anticyclone over southeastern China, and finally to see a cyclone over the Western Pacific (Fig. 5b).

In contrast, the increased stationary eddy vertical motion, that contributed to the greater increase in vertical moisture transport during the LGM (Fig. 6, right panel) compared with the pre-industrial period (Fig. 6, left panel) was identified as

the result of diabatic heating ($\overline{F^{net}}$) over the additional land mass area (ocean adjacent to Northeastern China in PI) due to the lower sea level at the LGM (Fig. 6, right panel) compared to pre-industrial period (Fig. 6, left panel). This remarkable heating center over the such region corresponds to an area of simulated rainfall increase during the LGM (Fig. 1d). However, we note the dominant role of $\overline{F^{net}}$ in inducing vertical motion changes at the LGM differs markedly from the similar determining role played by the horizontal advection of moist
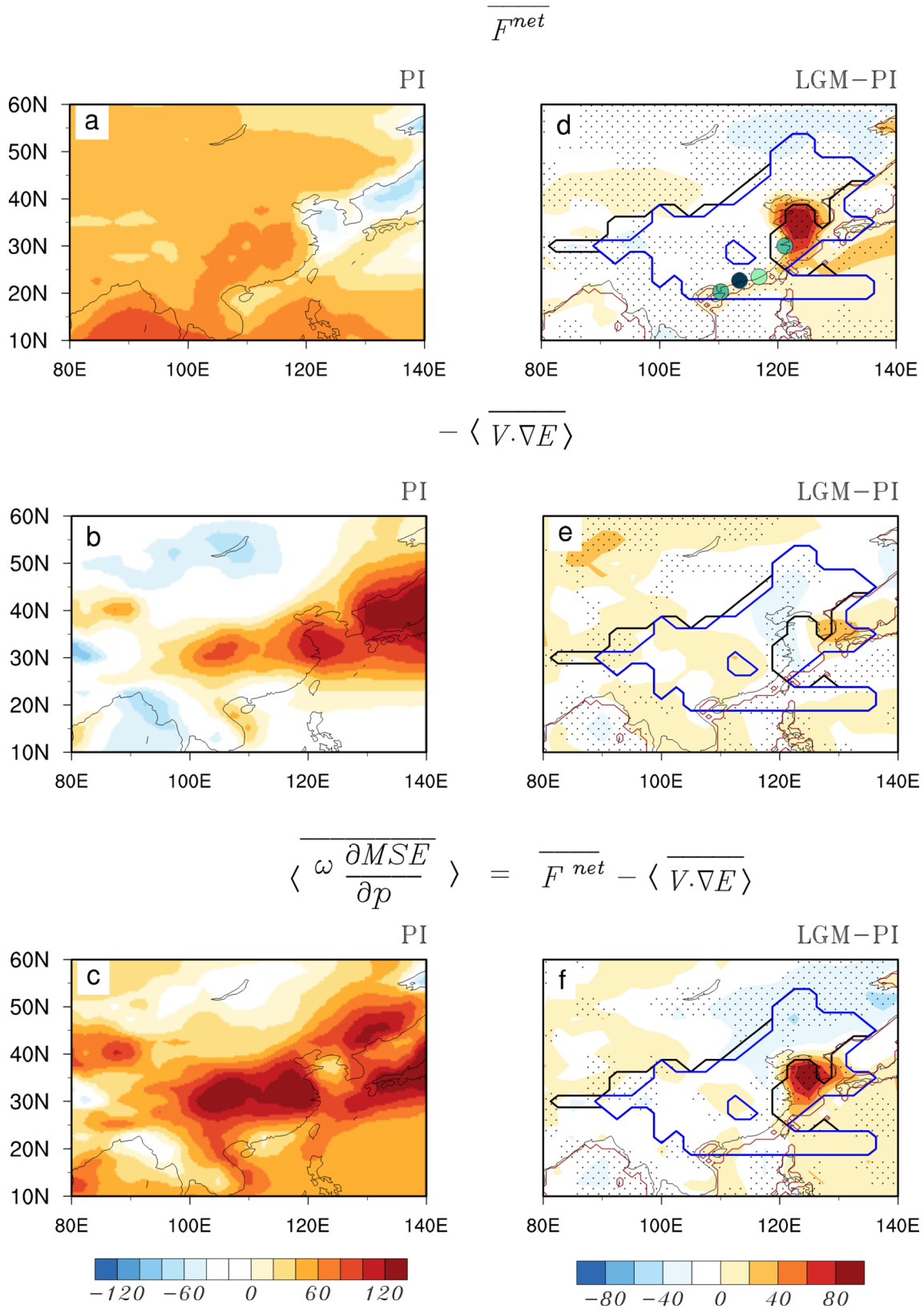
$$\overline{F^{net}}$$

PI LGM−PI

$$- \langle \overline{V \cdot \nabla E} \rangle$$

PI LGM−PI

$$\langle \overline{\omega \frac{\partial MSE}{\partial p}} \rangle = \overline{F^{net}} - \langle \overline{V \cdot \nabla E} \rangle$$

PI LGM−PI

◀**Fig. 6** The MME local and remote energy terms of the MSE budget equation formulated to analyse vertical motion (units: W m^{-2}) for JJA in PI (left panel), and the differences between LGM and PI (right panel). Top row: the net heat flux into the atmospheric column ($\overline{F^{net}}$, local energy). Middle row: the horizontal advection of moist enthalpy ($-\langle \overline{V \cdot \nabla E} \rangle$, remote energy). Bottom row: vertical advection of MSE calculated as the sum of $\overline{F^{net}}$ and $-\langle \overline{V \cdot \nabla E} \rangle$. Green circles in **d** indicate 4 proxy records with precipitation increase matching the dynamic process. The brown contour in right panel is the land-sea mask during LGM. The dotted areas at right panels are significance above the 5% level (Student's t-test)

enthalpy ($-\langle \overline{V \cdot \nabla E} \rangle$) under the past (mid-Piacenzian) and future (ECP4.5 scenario, extended RCP 4.5 pathway) warm climate scenarios (Sun et al. 2016, 2018). Such different causes of enhanced vertical motion in warm (mid-Piacenzian and ECP4.5 scenario) and cold (LGM) climates (1) indicate relative importance of $\overline{F^{net}}$ (local heating) and $-\langle \overline{V \cdot \nabla E} \rangle$ (remote heating transport) in inducing regional vertical motion are dependent on climate backgrounds (2) make stationary eddy horizonal circulation via two different ways contribute to EASM precipitation increase in warm and cold climates. One was identified as enhancement of vertical motion mainly induced by warm advection via $\langle \overline{V}^* \rangle$ in two warm climates (deduction from the highly simplification of $-\langle \overline{V \cdot \nabla E} \rangle$) (Sun et al. 2018); and the other as revealed by increased moisture advection of stationary eddy horizonal circulation in LGM (Fig. 5b).

3.4 Implications for reconciling model–data discrepancies

Given the opposing impacts of the TC and DC on EASM precipitation changes during the LGM (Fig. 2c) and the inconsistent signs of precipitation differences among the proxy records (Fig. 1d), one instinctive deduction is that the precipitation reconstructions show spatial variability in their ability to capture these two contrasting influences. That is, sites over central and northern China, showing precipitation decline, could reflect the dominant control of TC (Figs. 1d; 5a: brown dots). In contrast, the remaining records with precipitation increase are generally consistent with a dynamic enhancement on the horizontal moisture advection (Figs. 3b–f and 5b, green circles), and dynamic increase in vertical moisture transport due to diabatic heating ($\overline{F^{net}}$) could also explain a few pollen records showing precipitation increase (Fig. 6d, green circles). Meanwhile diabatic heating ($\overline{F^{net}}$) induced dynamic increase in vertical moisture transport is identified as dominant contributor to significant increase in the simulated precipitation along the exposed landmass area due to sea level drop during LGM (Figs. 1d and 6d).

4 Summary and conclusions

This study used paleoclimatic reconstructions and numerical simulations to analyze the East Asian monsoon changes during the LGM. The strong thermal climate features of the LGM contrast with those of the current anthropogenically induced warming climate (Sun et al. 2018). Our physical interpretation provides a new insight into the monsoon dynamics and shows that the LGM monsoon climate is far from the inverse of past and future warm climates. This finding improves our understanding of the dynamic complexity of monsoon evolution from past into future. Our key findings are summarized as follows.

1. A climate that was drier in China during the LGM than the pre-industrial period was confirmed by our quantitative data-model comparison over China. The signs of precipitation changes from various records generally follow the two contrasting physical processes, as revealed by a decomposition of the thermodynamic and dynamic water vapor budgets, which make opposing contributions to precipitation decline.
2. Thermodynamic processes dominate in the explanation of the decrease of EASM precipitation in data and models at the LGM. As climate cools, the water vapor holding capacity of air decreases with temperature (according to C–C relation). This leads to decrease of EASM precipitation during the LGM under thermal control mainly due to decrease in vertical moisture transport.
3. In contrast, there are distinct regions for EASM precipitation increase between data and models, which are regulated by two different dynamic processes. Both dynamic processes are mainly related to stationary eddy activity. Reconstructed precipitation increase in pollen records is explained by the strengthening role of stationary eddy horizontal circulation in horizontal moisture transport in the LGM (i.e., dynamic increase in horizontal moisture transport). The enhancement of stationary eddy vertical velocity strengthens the vertical moisture transport and thus increases the LGM-simulated precipitation over the exposed landmass along the continental coastline of China due to sea level drop during LGM (i.e., dynamic increase in vertical moisture transport).
4. There are also distinct regions for the relative magnitude of dynamic wetting and thermodynamic drying mechanisms in the simulations. The net decreases in precipitation are observed over the most part of EASM domain where thermodynamic decreases exceed the dynamic increases in precipitation. This finding is consistent with our previous statement that an overall drier LGM (relative to the pre-industrial period) EASM climate in data and models is mainly under the thermo-

dynamic control. Data-model comparison also shows that dynamic wetting mechanism is overpowered by the thermodynamic drying over data-model disagreement regions where models show net decrease and some data show net increase. Nevertheless, dynamic wetting and thermodynamic drying mechanisms could explain the spatial spread of reconstructed precipitation changes in sign. Meanwhile, thermodynamic drying mechanism is overwhelmed by dynamic wetting over the additional land mass area due to sea level drop during the LGM.

5. The relative importance of remote energy advection and local diabatic heating in inducing monsoonal vertical motion during LGM differs from the relative role of those in warm climates. Remote warm air advection undertaken by stationary eddy horizontal circulation acts the dominant role in inducing vertical motion increase in past (mid-Piacenzian) and future (ECP4.5 scenario) warm climates. In contrast, local diabatic heating (due to radiative heat flux and turbulent heat flux) is the main driver of intensified vertical motion at the LGM and is identified as the other contributor to an increase in EASM precipitation during the LGM.

References

Adam O, Schneider T, Enzel Y, Quade J (2019) Both differential and equatorial heating contributed to African monsoon variations during the mid-Holocene. Earth Planet Sci Lett 522:20–29. https://doi.org/10.1016/j.epsl.2019.06.019

Abe-Ouchi A, Saito F, Kageyama M, Braconnot P, Harrison SP, Lambeck K, Otto-Bliesner BL, Peltier WR, Tarasov L, Peterschmitt J-Y, Takahashi K (2015) Ice-sheet configuration in the CMIP5/PMIP3 last glacial maximum experiments. Geosci Model Dev Discuss 8:4293–4336. doi: https://doi.org/10.5194/gmdd-8-4293-2015

Bartlein PJ, Harrison S, Brewer S, Connor S, Davis BAS, Gajewski K, Guiot J, Harrison-Prentice TI, Henderson A, Peyron O, Prentice IC, Scholze M, Seppä H, Shuman B, Sugita S, Thompseon RS, Viau AE, Williams J, Wu H (2011) Pollen-based continental climate reconstructions at 6 and 21 ka: a global synthesis. Clim Dyn 37:775–802. https://doi.org/10.1007/s00382-010-0904-1

Braconnot P et al (2012) Evaluation of climate models using palaeoclimatic data. Nat Clim Change 2:417. https://doi.org/10.1038/nclimate1456

Braconnot P, Otto-Bliesner B, Harrison S, Joussaume S, Peterchmitt J-Y, Abe-Ouchi A, Crucifix M, Driesschaert E, Fichefet Th, Hewitt CD, Kageyama M, Kitoh A, Laine A, Loutre M-F, Marti O, Merkel U, Ramstein G, Valdes P, Weber SL, Yu Y, Zhao Y (2007a) Results of PMIP2 coupled simulations of the Mid-Holocene and last glacial maximum—part 1: experiments and large-scale features. Clim Past 3:261–277

Braconnot P, Otto-Bliesner B, Harrison S, Joussaume S, Peterchmitt J-Y, Abe-Ouchi A, Crucifix M, Driesschaert E, Fichefet Th, Hewitt CD, Kageyama M, Kitoh A, Loutre M-F, Marti O, Merkel U, Ramstein G, Valdes P, Weber L, Yu Y, Zhao Y (2007b) Results of PMIP2 coupled simulations of the Mid-Holocene and last glacial maximum—Part 2: feedbacks with emphasis on the location of the ITCZ and mid- and high latitudes heat budget. Clim Past 3:279–296

Burls N, Fedorov AV (2017) Wetter subtropics in a warmer world: contrasting past and future hydrological cycles. PNAS. https://doi.org/10.1007/s00382-016-3435-6

Cao J, Wang B, Liu J (2019) Attribution of the last glacial maximum climate formation. Clim Dyn 53:1661–1679. https://doi.org/10.1007/s00382-019-04711-6

Gao Y, Liu Z, Lu Z (2020) Dynamic Effect of Last Glacial Maximum Ice Sheet Topography on the East Asian Summer Monsoon. J Clim 33:6929–6944. https://doi.org/10.1175/JCLI-D-19-0562.1

Chen J, Bordoni S (2014) Orographic effects of the Tibetan Plateau on the East Asian summer monsoon: an energetic perspective. J Clim 27:3052–3072. https://doi.org/10.1175/JCLI-D-13-00479.1

Chevalier M, Brewer S, Chase BM (2017) Qualitative assessment of PMIP3 rainfall simulations across the eastern African monsoon domains during the mid-Holocene and the last glacial maximum. Quat Sci Rev 156:107–120. https://doi.org/10.1016/j.quascirev.2016.11.028

Chou C, Lan C-W (2012) Changes in the annual range of precipitation under global warming. J Clim 25:222–235

Clark PU, Alley RB, Pollard D (1999) Northern Hemisphere ice-sheet influences on global climate change. Science 286:1104–1111

Clark PU, Lix AC (2002) Ice sheets and sea level of the Last Glacial Maximum Quat. Sci Rev 21:1–7

Clark PU et al (2009) The Last Glacial Maximum. Science 325:710–714

CLIMAP Project Members (1976) The Surface of the Ice-Age Earth. Science 191:1131–1137

Farrera I, Harrison SP, Prentice IC, Ramstein G, Guiot J, Bartlein PJ, Bonnefille R, Bush M, Cramer W, von Grafenstein U, Holmgren

K, Hooghiemstra H, Hope G, Jolly D, Lauritzen SE, Ono Y, Pinot S, Stute M, Yu G (1999) Tropical climates at the Last Glacial Maximum: a new synthesis of terrestrial palaeoclimate data. I. Vegetation, lake-levels and geochemistry. Clim Dyn 15:823–856

Guiot J, Torre F, Jolly D, Peyron O, Boreux JJ, Cheddadi R (2000) Inverse vegetation modeling by Monte Carlo sampling to reconstruct palaeoclimates under changed precipitation seasonality and CO2 conditions: application to glacial climate in Mediterranean region. Ecol Model 127:119–140

Harrison SP et al (2015) Evaluation of CMIP5 palaeo-simulations to improve climate projections. Nat Clim Change 5:735. https://doi.org/10.1038/nclimate2649

Izumi K, Bartlein PJ (2016) North American paleoclimate reconstructions for the last glacial maximum using an inverse modeling through iterative forward modeling approach applied to pollen data. Geophys Res Lett 43:10965–10972. https://doi.org/10.1002/2016GL070152

Jahn A, Claussen M, Ganopolski A, Brovkin V (2005) Quantifying the effect of vegetation dynamics on the climate of the Last Glacial Maximum. Clim Past 1:1–7

Jiang D, Lang X (2010) Last Glacial Maximum East Asian monsoon: results of PMIP simulations. J Clim 23:5030–5038

Jiang D, Tian Z, Lang X, Kageyama M, Ramstein G (2015) The concept of global monsoon applied to the last glacial maximum: A multi-model analysis. Quat Sci Rev 126:126–139

Kageyama M, Peyron O, Pinot S, Tarasov P, Guiot J, Joussaume S, Ramstein G (2001) The last glacial maximum climate over Europe and western Siberia: a PMIP comparison between models and data. Clim Dyn 17(1):23–43

Kageyama M, Laîné A, Abe-Ouchi A, Braconnot P, Cortijo E, Crucifix M, de Vernal A, Guiot J, Hewitt CD, Kitoh A, Kucera M, Marti O, Ohgaito R, Otto-Bliesner B, Peltier WR, Vettoretti G, Weber SL, MARGO project members, (2006) Last Glacial Maximum temperatures over the North Atlantic, Europe and western Siberia: a comparison between PMIP models, MARGO sea-surface temperatures and pollen-based reconstructions. Quat Sci Rev 25:2082–2102

Kageyama M, Braconnot P, Bopp L, Caubel A, Foujols MA, Guilyardi E, Khodri M, Lloyd J, Lombard F, Mariotti V, Marti O, Roy T, Woillez MN (2013) Mid-Holocene and Last Glacial Maximum climate simulations with the IPSL model. Part II: model-data comparisons Clim Dyn. https://doi.org/10.1007/s00382-012-1499-5

Kageyama M et al (2017) The PMIP4 contribution to CMIP6—Part 4: scientific objectives and experimental design of the PMIP4–CMIP6 Last Glacial Maximum experiments and PMIP4 sensitivity experiments. Geosci Model Dev 10:4035–4055. https://doi.org/https://doi.org/10.5194/gmd-10-4035-2017

Kaplan JO (2001) Geophysical Applications of Vegetation Modeling. Ph.D. Thesis, Lund University, Lund

Korty RL, Camargo SJ, Galewsky J (2012) Tropical cyclone genesis factors in simulations of the Last Glacial Maximum. J Clim 25:4348–4365. https://doi.org/10.1175/JCLI-D-11-00517.1

Li X, Ting M (2017) Understanding the Asian summer monsoon response to greenhouse warming: the relative roles of direct radiative forcing and sea surface temperature change. Clim Dyn 49(7–8):2863–2880

Lin Y et al (2019) Mid-Holocene climate change over China: model–data discrepancy. Clim Past 15:1223–1249

Liu Z, Shin S, Otto-Bliesner BL, Kutzbach JE, Brady EC, Lee DE (2002) Tropical cooling at the last glacial maximum and extratropical ocean ventilation. Geophys Res Lett 29. doi: https://doi.org/10.1029/2001GL013938

Lu HY et al (2013) Variation of East Asian monsoon precipitation during the past 21 k.y. and potential CO2 forcing. Geology 41:1023–1026

Ludwig P, Schaffernicht EJ, Shao Y, Pinto JG (2016) Regional atmospheric circulation over Europe during the Last Glacial Maximum and its links to precipitation. J Geophys Res 121:2130–2145

Ludwig P, Gómez-Navarro JJ, Pinto JG, Raible CC, Wagner S, Zorita E (2019) Perspectives of regional paleoclimate modeling. Ann NY Acad Sci 1436:54–69. https://doi.org/10.1111/nyas.13865

MARGO Project Members (2009) Constraints on the magnitude and patterns of ocean cooling at the Last Glacial Maximum. Nat Geosci 2:127–132

Members of China Quaternary Pollen Data Base (MCQPD) (2000) Pollen-based Biome Reconstruction at Middle Holocene (6 ka BP) and Last Glacial Maximum (18 ka BP) in China. J Integr Plant Biol 42:1201–1209 ((**In Chinese with English abstract**))

Monnin E, Indermühle A, Dällenbach A, Flückiger J, Stauffer B, Stocker TF, Raynaud D, Barnola J-M (2001) Atmospheric CO2 concentrations over the last glacial termination. Science 291:112–114

Otto-Bliesner BL, Brady EC, Clauzet G, Tomas R, Levis S, Kothavala Z (2006) Last glacial maximum and holocene climate in CCSM3. J Clim 19:2526–2544

Peteet DM (2018) The importance of understanding the Last Glacial Maximum for climate change. In Our Warming Planet: Topics in Climate Dynamics. C. Rosenzweig, D. Rind, A. Lacis, and D. Manley, Eds., Lectures in Climate Change: Volume 1. World Scientific, pp. 331–348, doi: https://doi.org/10.1142/9789813148796_0016

Ramstein G, Kageyama M, Guiot J, Wu H, Hély C, Krinner G, Brewer S (2007) How cold was europe at the last glacial maximum? a synthesis of the progress achieved since the first pmip model-data comparison. Clim Past 3:331–339

Seager R, Naik N, Vecchi GA (2010) Thermodynamic and dynamic mechanisms for large-scale changes in the hydrological cycle in response to global warming. J Clim 23:4651–4668

Shakun JD et al (2012) Global warming preceded by increasing carbon dioxide concentrations during the last deglaciation. Nature 484:49–54

Sun Y, Zhou T, Ramstein G, Contoux C, Zhang Z (2016) Drivers and mechanisms for enhanced summer monsoon precipitation over East Asia during the mid-Pliocene in the IPSL-CM5A. Clim Dyn 46:1437–1457

Sun Y, Ramstein G, Li L, Contoux C, Tan N, Zhou T (2018) Quantifying East Asian summer monsoon dynamics in the ECP4.5 scenario with reference to the mid-Piacenzian warm period. Geophys Res Lett 45:12523–12533. https://doi.org/10.1029/2018GL080061

Trenberth KE, Guillemot CJ (1995) Evaluation of the global atmospheric moisture budget as seen from analyses. J Clim 8:2255–2272

Wang B, Liu J, Kim HJ, Webster PJ, Yim SY (2012) Recent change of the global monsoon precipitation (1979–2008). Clim Dyn 39:1123–1135

Wu H, Guiot J, Brewer S, Guo Z (2007) Climatic changes in Eurasia and Africa at the last glacial maximum and mid-Holocene: reconstruction from pollen data using inverse vegetation modelling. Clim Dyn 29(2):211–229. https://doi.org/10.1007/s00382-007-0231-3

Wu H, Li Q, Yu Y, Sun A, Lin Y, Jiang W, Luo Y (2019) Quantitative climatic reconstruction of the Last Glacial Maximum in China. Sci China Earth Sci 62:1269–1278. https://doi.org/10.1007/s11430-018-9338-3

Yan M, Wang B, Liu J (2016) Global monsoon change during the Last Glacial Maximum: a multi-model study. Clim Dyn 47:359–374

Yan Q, Zhang Z (2017) Dominating roles of ice sheets and insolation in variation of tropical cyclone genesis potential over the north atlantic during the last 21,000 years. Geophys Res Lett 44:10624–10632. https://doi.org/10.1002/2017GL075786

Yanase W, Abe-Ouchi A (2007) The LGM surface climate and atmospheric circulation over East Asia and the North Pacific in the PMIP2 coupled model simulations. Clim Past 3:439–451

Zheng YQ, Yu G, Wang SM, Xue B, Zhuo DQ, Zeng XM, Liu HQ (2004) Simulation of paleoclimate over East Asia at 6 ka BP and 21 ka BP by a regional climate model. Clim Dyn 23:513–529

Affiliations

Yong Sun[1,2] · **Haibin Wu**[3,4,5] · **Masa Kageyama**[2] · **Gilles Ramstein**[2] · **Laurent Z. X. Li**[6] · **Ning Tan**[3] · **Yating Lin**[3] · **Bo Liu**[7,1] · **Weipeng Zheng**[1,8] · **Wenchao Zhang**[3] · **Liwei Zou**[1] · **Tianjun Zhou**[1,9]

[1] State Key Laboratory of Numerical Modeling for Atmospheric Sciences and Geophysical Fluid Dynamics, Institute of Atmospheric Physics, Chinese Academy of Sciences, Beijing 100029, China

[2] Laboratoire des Sciences du Climat et de L'Environnement, LSCE/IPSL, CEA-CNRS-UVSQ, Université Paris-Saclay, Gif-sur-Yvette, France

[3] Key Laboratory of Cenozoic Geology and Environment, Institute of Geology and Geophysics, Chinese Academy of Sciences, Beijing 100029, China

[4] CAS Center for Excellence in Life and Paleoenvironment, Beijing 100044, China

[5] University of Chinese Academy of Sciences, Beijing 100049, China

[6] Laboratoire de Météorologie Dynamique, CNRS, Sorbonne Université, Ecole Normale Supérieure, Ecole Polytechnique, Paris, France

[7] Department of Atmospheric Science, School of Environmental Studies, China University of Geoscience, Wuhan 430074, China

[8] College of Earth and Planetary Sciences, University of Chinese Academy of Sciences, Beijing 100049, China

[9] CAS Center for Excellence in Tibetan Plateau Earth Sciences, Chinese Academy of Sciences (CAS), Beijing 100101, China